

# Programmable optical parametric amplifier synthesizer for cubic phase states and amplified Schrodinger cat states

Yusuf Turek,<sup>\*</sup> Ming-Yan Sun<sup>§</sup>, and Xiao-Xi Yao<sup>§</sup>  
*School of Physics, Liaoning University, Shenyang, Liaoning 110036, China*  
(Dated: July 1, 2026)

We introduce a programmable optical parametric amplifier (OPA) synthesizer that, under a heralded photon-number-resolving framework, generates high-fidelity cubic phase states and amplifies Schrodinger cat states. By systematically exploring both the catalytic configuration, where the idler input and output contain the same number of photons ( $m = n$ ), and non-catalytic configurations ( $m \neq n$ ), we discover two qualitatively different functionalities. First, with a coherent-state signal input, our protocol generates cubic phase states with fidelity exceeding 0.99 across a broad range of ( $m, n$ ) configurations. Second, using a Schrodinger cat state as the signal input, the same framework amplifies the cat state: an input cat with amplitude  $\alpha_{in} \leq 1$  is transformed into an output squeezed cat with  $\alpha_{out} \geq 2$  while maintaining fidelity above 0.99. The catalytic configuration preserves the input parity and restores the idler state, whereas non-catalytic configurations enable parity-flipping amplification with higher success rates. Moreover, the amplified output can serve as a seed for subsequent amplification rounds, offering a self-seeding pathway to progressively larger cat states. Our protocol requires only moderate-gain OPA operation and low-order photon-number-resolving detection, providing a flexible and experimentally accessible platform for cubic phase state preparation and amplified squeezed cat state generation.

## I. INTRODUCTION

The ability to generate and manipulate non-Gaussian states of light is a cornerstone of continuous-variable quantum information processing, enabling universal quantum computation [1, 2], fault-tolerant error correction [3, 4], and quantum metrology beyond the standard quantum limit [5–11]. Among the most sought-after non-Gaussian resources are cubic phase states, which provide the nonlinearity required for the cubic phase gate – a key missing element for universal Gaussian-only architectures [12–14].

A promising approach for producing non-Gaussian states uses an optical parametric amplifier (OPA) with heralded photon detection. Shringarpure and Franson first demonstrated that an OPA seeded with a coherent state and a single idler photon can generate photon-added states [15]. More recently, Erkilic et al. showed that with vacuum idler input ( $m = 0$ ) and heralded photon detection, an OPA can produce cubic-phase-like states with fidelities exceeding 98.5% [16]. In these schemes, however, the idler port is restricted to either vacuum or a fixed Fock state.

Furthermore, our recent work has established that this OPA heralding architecture is more than a state generator—it is the kernel of a reconfigurable quantum state synthesizer [17, 18]. By varying the idler photon numbers ( $m, n$ ), the same device implements effective high-order photon subtraction from a squeezed vacuum, producing large-amplitude cat states with controllable parity [18]. These operations constitute the synthesizer’s

base modes. However, whether this platform can generate entirely new classes of states—such as cubic phases—or amplify non-Gaussian seeds remains an open question.

Here we fill both gaps—systematically investigating the full ( $m, n$ ) parameter space, exploring both catalytic ( $m = n$ ) and non-catalytic ( $m \neq n$ ) configurations. As we demonstrate below, this unified framework yields two qualitatively new effects that are absent in all previous OPA schemes—including our own base-mode operations [17, 18].

First, using a coherent state as the signal input, we find that high-fidelity cubic phase states ( $F \geq 0.99$ ) can be generated across a broad range of ( $m, n$ ) configurations—not only under the catalytic condition but also in non-catalytic settings. This result is non-trivial: coherent states are Gaussian, while cubic phase states are highly non-Gaussian, and no linear optical transformation can bridge the two. The OPA heralding framework thus provides a compact, integrated nonlinear channel that accomplishes this conversion using only photon-number-resolving detection.

Second, using an unsqueezed Schrodinger cat state as the signal input, the same protocol amplifies the cat state: an input cat with amplitude  $\alpha_{in} \leq 1$  is transformed into a squeezed cat state with  $\alpha_{out} \geq 2$  while maintaining fidelity above 0.99. This constitutes both amplitude amplification and the generation of squeezing—two effects simultaneously achieved in a single heralding step. Large-amplitude squeezed cat states are essential resources for fault-tolerant bosonic error correction [19, 20], yet their preparation remains challenging. Our protocol offers a direct and experimentally accessible route to such states starting from a small unsqueezed cat, which is significantly easier to generate [21, 22].

Notably, the catalytic configuration  $m = n$  preserves

<sup>§</sup> These authors contributed equally to this work.

<sup>\*</sup> Corresponding author: [yusufu1984@hotmail.com](mailto:yusufu1984@hotmail.com)

the input parity and restores the idler state, whereas non-catalytic configurations  $m \neq n$  enable parity-flipping amplification with higher success probabilities. This flexibility allows the protocol to be tailored for different quantum information tasks, establishing a programmable and unified platform for non-Gaussian state engineering.

A critical question is whether the present work merely repeats the architecture of previous studies with a different input state. We emphasize that this is not the case. While the OPA architecture is shared with Refs. [15–18], the physical effects reported here are qualitatively different. Reference [16] restricted the idler input to vacuum ( $m = n = 0$ ) and did not explore the catalysis condition  $m = n$  for coherent inputs, nor did it consider arbitrary non-catalytic configurations ( $m \neq n$ ) or cat state inputs at all. Thus, this work is neither a trivial extension nor a parameter scan; it uncovers a unified and programmable OPA platform for non-Gaussian state engineering that was previously inaccessible.

The paper is organized as follows. Section II describes the general OPA heralding formalism for arbitrary idler input and output photon numbers. Section III presents cubic phase state generation from coherent state inputs under various configurations. Section IV demonstrates squeezed cat state amplification from unsqueezed cat state inputs. In Sect. V, we discuss effects of photon loss on system quantities including fidelity, Winger negativity and complexity. We conclude our paper in Sect. VI. Numerical simulations of this work are done using QuTiP [23].

## II. THE NON-GAUSSIAN STATE SOURCE

The schematics of our state generation protocol is showed in Fig. 1. Our protocol employs an optical parametric amplifier (OPA) with two input ports: the signal port, which carries the input state  $|\psi\rangle$  (either a coherent state or a Schrodinger cat state in this present work), and the idler port, which is prepared in a Fock state  $|m\rangle$  with a definite photon number  $m$ . The OPA interaction, characterized by a tunable gain parameter  $g$ , entangles the two modes and induces photon transfers between them. At the idler output, we perform photon-number resolving detection and postselect events in which exactly  $n$  photons are detected, where  $n$  can be any non-negative integer, not necessarily equal to  $m$ . This conditional measurement projects the signal mode into a non-Gaussian state.

The action of the OPA can be described by the two-mode squeezing operator

$$S(\tau) = \exp(\tau^* ab - \tau a^\dagger b^\dagger), \quad (1)$$

where  $\tau = \rho e^{i\delta}$  and  $g = \cosh \rho$  denote the non-linear and gain parameters of the OPA,  $G = \tanh \tau = \sqrt{g^2 - 1}/g$ , and  $a$  ( $a^\dagger$ )  $b$  ( $b^\dagger$ ) are the annihilation (creation) operators of signal and idler modes, respectively. The normal



Figure 1. Schematics of our protocol. Idler mode with Fock state  $|m\rangle$  and signal in state  $|\phi\rangle$  plugged into an optical parametric amplifier (OPA). Heralding  $m$ -photon idler output gives state  $|\Phi\rangle$  in signal output.

ordered decomposition of  $S(\tau)$  can be written as

$$S(\tau) = \frac{1}{g} e^{-Ga^\dagger b^\dagger} g^{-(a^\dagger a + b^\dagger b)} e^{Gab}. \quad (2)$$

The initial joint state is chosen as  $|\phi\rangle \otimes |m\rangle$ , with an arbitrary signal state  $|\phi\rangle$  and a Fock state  $|m\rangle$  in the idler. After the OPA interaction, a photon-number-resolving measurement on the idler mode postselects the outcome  $n$ , which projects the signal mode into the unnormalised state  $|\psi\rangle_{\psi,m,n} = \langle n|S(\tau)|\phi\rangle|m\rangle$ . To evaluate this expression, we apply the three factors of the decomposition successively to the initial state and keep only the terms that lead to exactly  $n$  photons in the idler. resulting expression takes the compact form

$$|\Psi\rangle_{\psi,m,n} = \sum_{k=0}^m H(k, m, n) (a^\dagger)^{n-m+k} g^{-a^\dagger a} a^k |\psi\rangle \quad (3)$$

where

$$H(k, m, n) = \frac{G^{n-m+2k}}{g^{m-k+1}} \frac{(-1)^{n-m+k} \sqrt{n!m!}}{k!(n-m+k)!(m-k)!}. \quad (4)$$

The power of  $G$  is obtained from the product  $G^k \cdot (-G)^{n-m+k}$ , and the denominator contains the factorials from the expansions as well as an extra power of  $g$  that originates from the idler attenuation and the initial  $1/g$ .

The heralded signal state in Eq. (3) is a coherent superposition over  $k = 0, \dots, m$  of terms in which the input state  $|\phi\rangle$  is sequentially processed by three operations: first,  $k$  photons are subtracted via  $a^k$ ; second, the resulting state undergoes noiseless attenuation through  $g^{-a^\dagger a}$ ; and third,  $n = m + k$  photons are added via  $(a^\dagger)^{n-m+k}$ . This right-to-left ordering is essential because the three operators do not commute, and it arises naturally from the normal-ordered decomposition of the two-mode squeezing unitary. Thus, the protocol implements a programmable sequence of photon subtraction, amplitude scaling, and photon addition, with the net photon-number change determined by the difference between the detected and input idler photon numbers.

The resulting heralded signal state  $|\Psi\rangle_{\psi,m,n}$  depends on the chosen parameters  $(m, n, g)$  and the input state.

By scanning these parameters, we can tailor the output to match various target non-Gaussian states. In this work, we demonstrate two prominent applications: for a coherent input, appropriate choices of  $(m, n, g)$  yield cubic phase states with fidelity exceeding 0.99, while for a cat-state input, the protocol transforms a small-amplitude unsqueezed cat into a larger-amplitude squeezed cat with extreme high fidelity. Notably, the catalytic case  $m = n$  is a special subclass that preserves the input parity and restores the idler state, but it is not the only working configuration; non-catalytic settings can also offer higher success probabilities. Thus, our scheme provides a general and programmable non-Gaussian state synthesizer, with arbitrary  $m, n$  offering flexible trade-offs between fidelity, success probability, and experimental resources, all depicted schematically in Fig. 1.

The norm square of this unnormalised state gives the success probability  $P_{m,n} = \text{Tr}(|\Psi\rangle_{\psi,m,n}\langle\Psi|)$  for the heralding event, which is the conditional probability that the idler output contains exactly  $n$  photons given that the idler input was prepared in  $|m\rangle$  and the signal input was  $|\psi\rangle$ . However, in a realistic experimental implementation, the total probability per trial for successfully generating the heralded state must also account for the probability of preparing the initial  $m$ -photon Fock state at the idler input. If this Fock state is generated by a separate spontaneous parametric down-conversion (SPDC) source with gain parameter  $g'$ , then the preparation probability is  $P_{\text{Fock}}(m, g') = |{}_s\langle m | (\mathbb{I} \otimes |m\rangle\langle m|) S(\tau') (|0\rangle_a \otimes |0\rangle_b) |^2$ . The overall success probability per trial is therefore the product of this Fock-state preparation probability, the conditional OPA heralding probability  $P_{m,n}$ , and the detection efficiency  $\eta_{\text{det}}$  of the photon-number-resolving detector:  $P_{\text{trial}} = \eta_{\text{det}} P_{\text{Fock}}(m, g') P_{m,n}$ . This factorization holds because the two heralding stages—Fock-state generation and OPA interaction—are independent when the idler mode is losslessly routed between them. So far, PNRDs with high quantum efficiency ( $\eta_{\text{det}} \geq 0.95$ ) have been reported [24–27]. Hence, in practice, the dominant contribution to low  $P_{\text{trial}}$  comes from either the Fock-state preparation (especially for large  $m$  where multiphoton SPDC is inefficient) or the OPA heralding probability (which decreases with increasing detected photon number  $n$ ). Despite these limitations, the single-trial probabilities we obtain are comparable to or even higher than those reported in other heralded non-Gaussian state generation schemes, and the low values for high- $m$  configurations can be overcome by operating the pump laser at high repetition rates [27–29]. In the following sections, we will present explicit results of  $P_{\text{trial}}$  for the specific configurations that generate cubic phase states and amplified cat states, demonstrating that our protocol is experimentally feasible with current technology.

Before analyzing specific input states, we recall the definitions of two important families of states that will be used throughout this work. A coherent state is obtained by applying the displacement operator  $D(\alpha) =$

$\exp(\alpha a^\dagger - \alpha^* a)$  to the vacuum:

$$|\alpha\rangle = D(\alpha)|0\rangle = e^{-|\alpha|^2/2} \sum_{p=0}^{\infty} \frac{\alpha^p}{\sqrt{p!}} |p\rangle. \quad (5)$$

A cat state is a superposition of two coherent states with opposite amplitudes and a relative phase:

$$|Cat\rangle_{\alpha,\theta} = N_\theta^{-1/2} (|\alpha\rangle + e^{i\theta} |-\alpha\rangle), \quad (6)$$

where  $N_\theta = 2 \left(1 + e^{-2\alpha^2} \cos\theta\right)$  ensures normalisation, and the even and odd cat states (ECS, OCS) correspond to  $\theta = 0$  and  $\theta = \pi$ , respectively.

As mentioned above the properties of output signal state  $|\Psi\rangle_{\psi,m,n}$  depends on the OPA gain  $g$ , the input and detected photon numbers  $m, n$ , and the input signal state  $|\psi\rangle$ . For general parameters the state is a complex superposition of many terms, but in certain limiting cases the expression simplifies considerably and admits a clear physical interpretation.

(i) When  $m = n = 0$ , the idler is initially in the vacuum and we postselect on zero photons at the output; the sum in Eq. (3) reduces to the single term  $k = 0$  yielding  $|\Psi\rangle_{\psi,0,0} \propto g^{-a^\dagger a} |\psi\rangle$ . As investigated in Ref. [30] this operation is known as noiseless attenuation. It scales the amplitude of every Fock component without changing the photon-number parity or introducing additional photons. For a coherent state input,  $g^{-a^\dagger a} |\alpha\rangle \propto |\alpha/g\rangle$ , so the output remains a coherent state with its amplitude reduced by a factor of  $g$ . For a cat state input, the same attenuation acts on each coherent component individually, producing  $|Cat\rangle_{\alpha/g,\theta}$  with the same relative phase  $\theta$  but a smaller amplitude.

(ii) For  $m = 0$  and  $n \neq 0$ , i.e., vacuum idler input but heralding on  $n$  photons, only the  $k = 0$  term survives and the output becomes  $|\Psi\rangle_{\psi,0,n} \propto (a^\dagger)^n g^{-a^\dagger a} |\psi\rangle$ . Thus the protocol effectively adds  $n$  photons to the input state after an attenuation, which is precisely the photon-added attenuated state studied in previous works [31–34].

(iii) In the complementary case  $m \neq 0$  and  $n = 0$ , the detected photon number is zero while the idler initially contains  $m$  photons. The condition  $n - m + k$  forces  $k = m$ , so only the last term of the sum contributes, giving  $|\Psi\rangle_{\psi,m,0} \propto g^{-a^\dagger a} a^m |\psi\rangle$ . This corresponds to  $m$ -photon subtraction followed by noiseless attenuation, a process that can generate non-Gaussian features such as Wigner negativity when applied to a suitable input state [21, 22, 35].

These three special cases already illustrate the versatility of the OPA heralding scheme: by choosing  $(m, n)$  we can implement noiseless attenuation, photon addition, or photon subtraction within a single unified framework. In the following sections, we will discuss in detail the cases where the signal input is a coherent state and a Schrodinger cat state, respectively, and demonstrate how the general heralded state  $|\Psi\rangle_{\psi,m,n}$  can be engineered

to produce high-fidelity cubic phase states and amplified squeezed cat states through appropriate choices of the parameters  $m$ ,  $n$  and the OPA gain  $g$ .

### III. CUBIC PHASE STATE GENERATION FROM COHERENT STATE INPUT

We first consider a coherent state input  $|\psi\rangle = |\alpha\rangle = D(\alpha)|0\rangle$ . Substituting into Eq. (3) using the identity  $g^{-a^\dagger a}|\alpha\rangle \propto |\alpha/g\rangle$ , we obtain the unnormalized heralded state

$$|\Psi\rangle_{coh,m,n} = \exp\left[-\frac{G^2|\alpha|^2}{2}\right] \sum_{k=0}^m H(k, m, n) \alpha^k (a^\dagger)^{n-m+k} \left|\frac{\alpha}{g}\right\rangle \quad (7)$$

where we have used  $a^k|\alpha/g\rangle = (\alpha/g)^k|\alpha/g\rangle$ , valid for a coherent state. Expanding the photon-addition operator  $(a^\dagger)^{n-m+k}$  in the Fock basis and applying the displacement operator  $D(\alpha/g)$ , the state can be rewritten in the compact form

$$|\Psi\rangle_{coh,m,n} = D\left(\frac{\alpha}{g}\right) \sum_{k=0}^m \sum_{l=0}^{n-m+k} C(m, n, k, l) |l\rangle, \quad (8)$$

with the coefficients

$$C(m, n, k, l) = \exp\left[-\frac{G^2|\alpha|^2}{2}\right] \times \frac{H(k, m, n) \alpha^k (n-m+k)! \left(\frac{\alpha^*}{g}\right)^{n-m+k-l}}{\sqrt{l!} (n-m+k-l)}. \quad (9)$$

This representation shows that the heralded state is a globally displaced superposition of Fock states, with the displacement amplitude reduced by the OPA gain factor  $g$ . The Wigner functions of  $|\Psi\rangle_{coh,m,n}$  for various  $(m, n)$  configurations with fixed  $g = 1.5$  are plotted in Fig. 2, where the emergence of negative regions—signatures of non-classicality—is clearly visible for configurations with non-zero photon addition.

When the model parameters are set to the symmetric case  $m = n$ , the general heralded state simplifies considerably and acquires a clear physical interpretation. The resulting unnormalized output state can be written as

$$|\Psi'\rangle_{coh,n,n} = D\left(\frac{\alpha}{g}\right) \sum_{l=0}^n \mathcal{C}_l |l\rangle, \quad (10)$$

where the coefficients  $\mathcal{C}_l = \sum_{k=l}^n C_{n,k,l}$  are given by

$$C_{n,k,l} = \exp\left[-\frac{G^2|\alpha|^2}{2}\right] \frac{1}{g^{n-l+1}} \frac{(-1)^k n! G^{2k} \alpha^k (\alpha^*)^{k-l}}{k!(n-k)! \sqrt{l!} (k-l)!}. \quad (11)$$

The output state in Eq. (10) represents a displaced, photon-number-truncated non-Gaussian state. Its structure — a coherent superposition of Fock states up to  $|n\rangle$  globally displaced by  $\alpha/g$  — is tunable via the scaling parameter  $g$ . Unlike standard photon-added coherent states [33], this state does not amplify the input coherent state for  $g > 1$ . Instead, it provides a flexible platform for generating non-Gaussian states with controllable photon-number distributions and Wigner-function negativity.

Among non-Gaussian resources, cubic phase states play a particularly important role in continuous-variable quantum information processing [12, 36]. A cubic phase state (CPS) is defined as

$$|\gamma'\rangle = e^{i\gamma'x^3} |0\rangle_p, \quad (12)$$

where  $\gamma' \in \mathbb{R}$  is the strength of the cubic nonlinearity (hereafter referred to as the cubicity),  $x = (a + a^\dagger)/\sqrt{2}$  is the position quadrature, and  $|0\rangle_p$  is the zero-momentum eigenstates. Since the ideal zero-momentum eigenstate is unphysical, experimentally realizable cubic phase states are typically prepared with finite squeezing:

$$|\Psi_{target}\rangle = e^{i\gamma'x^3} S(r) |0\rangle, \quad (13)$$

where  $S(r) = \exp\left[\frac{r^2}{2}(a^2 - a^{\dagger 2})\right]$  the squeezing operator and  $r \in \mathbb{R}$  is the squeezing parameter. All squeezing values  $r$  used in this work can be converted to the decibel (dB) scale using the formula  $r_{dB} = \frac{20}{\ln 10} r \approx 8.686r$ . Cubic phase states are essential resources for universal continuous-variable quantum computation, as they enable the implementation of the cubic phase gate  $e^{i\gamma'x^3}$  which, together with Gaussian operations, forms a universal gate set [36]. Despite their importance, generating high-fidelity cubic phase states has remained a long-standing challenge.

So far several approaches have been proposed to effectively generate cubic phase states. Arzani et al. [37] proposed cascaded measurement protocols to cubic phase states using single-photon detection, but the success probability decreases rapidly with the number of required steps. Kerr nonlinearity has been explored as a route to the cubic phase gate [38, 39], but its weak strength at the single-photon level has motivated alternative approaches using Gaussian enhancement [39] or conditional state preparation [38]. Gaussian conversion protocols transform a pre-existing non-Gaussian state—the trisqueezed state—into a cubic phase state using only squeezing and displacement, achieving fidelities up to  $F = 0.997$ , but this approach requires a complex non-Gaussian seed generated by challenging three-photon down-conversion techniques [14]. Interferometer-based heralded schemes have been explored using a Fock state  $|2\rangle$  and a coherent state as inputs, followed by projection onto  $|2\rangle$ . Kashyap et al. [40] demonstrated that such a scheme can generate cubic phase states with fidelity  $F \sim 0.99$ , but at an extremely low success probability  $P \sim 10^{-7}$  when high fidelity is required. Balancing the beamsplitter to improve the success probability reduces the fidelity to  $F \sim 0.97$ .

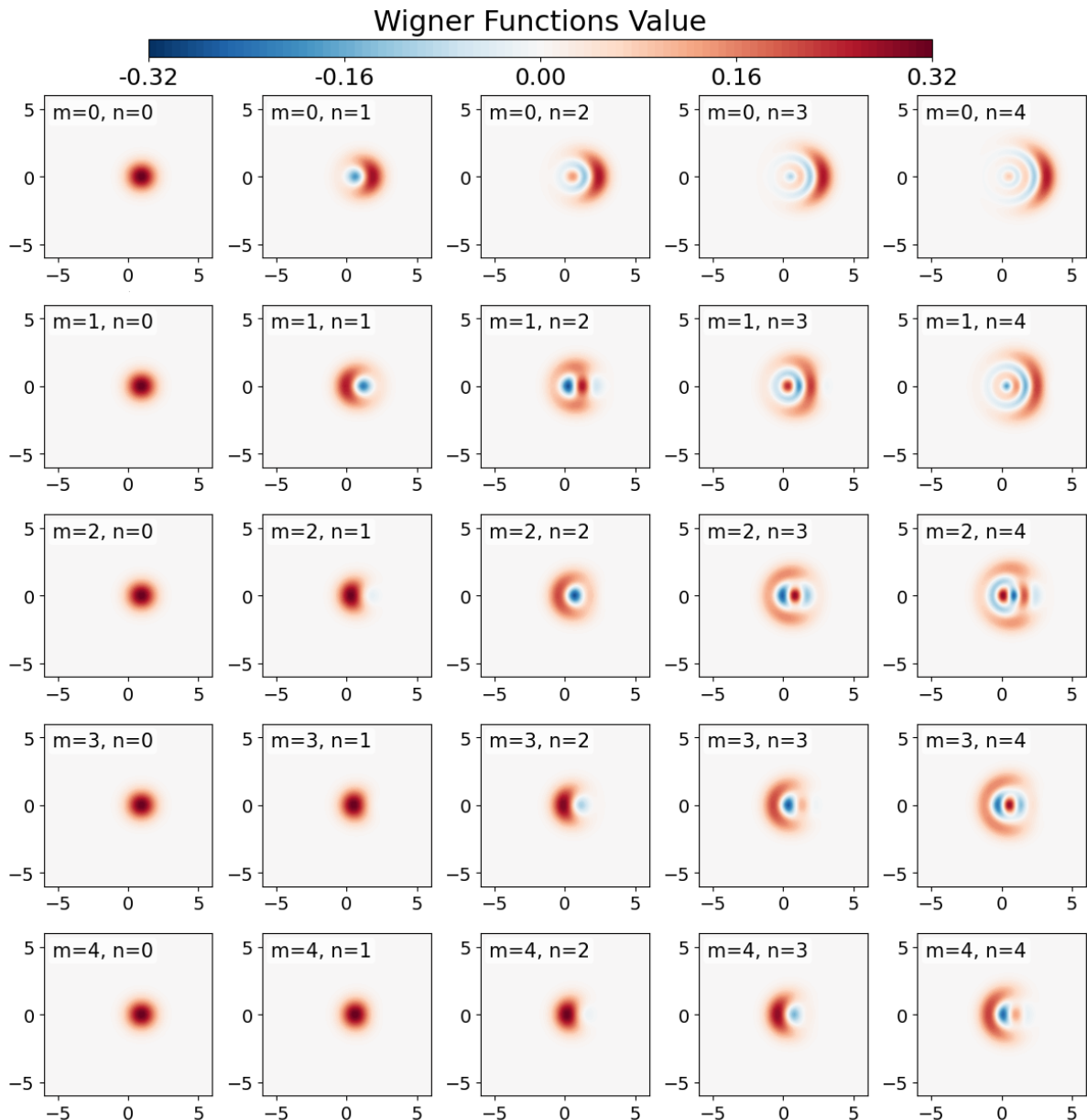


Figure 2. Wigner functions of the heralded signal  $|\Psi'\rangle_{coh,n,n}$  for coherent state input with various configurations  $(m, n)$ , with fixed  $\alpha = 1$  and  $g = 1.5$ . The emergence of negative regions indicates non-classicality.

Most recently, Erkilic et al. [34] demonstrated a significant advance to generate CPS using an OPA with heralded photon detection. In their scheme, the idler port is seeded with vacuum ( $m = 0$ ), while a coherent state is injected into the signal port. By performing photon-number-resolving detection on the idler output and heralding on  $n$  photons ( $n \geq 1$ ), they showed that cubic-phase-like states can be generated with fidelities exceeding 98.5%. This work is notable because it generates non-Gaussian states using only Gaussian inputs (coherent states) and a single OPA, without requiring pre-existing non-Gaussian resources such as Fock states or trisqueezed states. However, the idler port in Erkilic

et al.'s scheme is restricted to vacuum input ( $m = 0$ ). The more general case where the idler is seeded with a Fock state ( $m \geq 1$ ) and in particular the catalysis configuration where the idler input and output contain the same number of photons ( $m = n$ ) was not explored.

In this work, we generalize the OPA heralding framework to arbitrary idler input Fock states ( $m \geq 0$ ) and arbitrary heralded photon numbers ( $n \geq 0$ ). We systematically investigate the full parameter space of  $(m, n)$  configurations and discover that cubic phase states can be generated across a wide range of configurations — not only under the catalysis condition  $m = n$ , but also for  $m \neq n$  cases.

Table I. Optimized parameters ( $g$ ,  $\gamma$ ,  $r$ ,  $\alpha$ ,  $r_{corr}$ ,  $\beta_{corr}$ , fidelity  $F$ , and success probability  $P_{trial}$ ) for cubic phase state generation from coherent state input for various  $(m, n)$  configurations.

$(m, n)$	$g$	$\gamma'$	$r$	$\alpha$	$r_{corr}$	$\beta_{corr}$	$F$	$P_{total}$
(0, 4)	1.46	0.103	0	$-2.145i$	0.521	$2.963i$	0.997	$8.28 \times 10^{-2}$
(1, 1)	1.08	0.100	0	$-4.136i$	0.203	$4.406i$	0.975	$1.17 \times 10^{-2}$
(1, 4)	1.15	0.146	-0.01	$-1.448i$	0.589	$2.493i$	0.989	$8.82 \times 10^{-3}$
(1, 5)	1.07	0.100	0	$-2.260i$	0.469	$3.401i$	0.991	$3.75 \times 10^{-4}$
(2, 2)	2.06	0.100	0	$-3.676i$	0.399	$2.786i$	0.993	$1.13 \times 10^{-5}$
(2, 5)	1.05	0.100	0	$-1.614i$	0.504	$2.703i$	0.995	$3.80 \times 10^{-4}$
(3, 3)	2.34	0.128	0	$-3.933i$	0.527	$3.020i$	0.992	$6.69 \times 10^{-7}$
(4, 4)	2.47	0.166	-0.01	$-3.960i$	0.647	$3.258i$	0.987	$1.19 \times 10^{-7}$

The optimisation procedure for generating cubic phase states proceeds as follows. For a given  $(m, n)$  configuration and input coherent amplitude  $\alpha$ , we compute the heralded state  $|\Psi\rangle_{coh,m,n}$  from Eq. (7) and then apply a squeezing operation  $S(r_{corr}) = \exp[\frac{r_{corr}}{2}(a^2 - a^{\dagger 2})]$  followed by a displacement  $D(\beta_{corr})$  to match the target cubic phase state  $|\Psi_{target}\rangle$ . The fidelity  $F = |\langle \Psi_{target} | S(r_{corr})D(\beta_{corr})|\Psi\rangle_{coh,m,n}|^2$  is maximised over the parameters ( $g$ ,  $\alpha$ ,  $r$ ,  $\gamma'$ ,  $r_{corr}$ ,  $\beta_{corr}$ ), where the OPA gain  $g$  and input amplitude  $\alpha$  determine the heralded state, while  $r_{corr}$  and  $\beta_{corr}$  are the Gaussian correction parameters, and  $\gamma'$  is the target cubicity. The numerical optimisation is performed using gradient-based methods implemented in QuTiP [23].

Table I presents the optimised parameters and resulting fidelities for several representative configurations. We first focus on the catalytic cases  $m = n$ , which are the central new contribution of this work. The configurations (1, 1), (2, 2), (3, 3), and (4,4) all yield fidelities close to or exceeding 0.99 with appropriately chosen OPA gains and input amplitudes. For comparison, we also include the (0,4) configuration which was previously studied by Erkilic et al. [34] and is included here as a reference; it achieves a fidelity of 0.997 with a significantly higher success probability of  $8.28 \times 10^{-2}$ . In addition to the catalytic and vacuum-input cases, we have identified several non-catalytic configurations with  $m \neq n$  and  $m \neq 0$  that also produce high-fidelity cubic phase states, such as (1, 4), (1, 5), and (2, 5), with fidelities of 0.989, 0.991, and 0.995, respectively. These results demonstrate that high-fidelity cubic phase states can be generated across a broad range of  $(m, n)$  configurations, not only under the catalytic condition but also in non-catalytic settings, offering flexibility in balancing fidelity and success probability. The target squeezing parameter  $r$  (fourth column) is near zero (approximately  $-0.01$  to  $0$ ) for all cases, indicating that the generated state is already close to the required squeezed form before the final Gaussian correction. This is a significant practical advantage, as it implies that only minimal additional squeezing is needed to reach the target state. This trend can also be seen from the Wigner function fringes in Fig. 2.

The Wigner functions of the optimised output states for the catalytic cases  $m = n = 1, 2, 3, 4$  are shown in

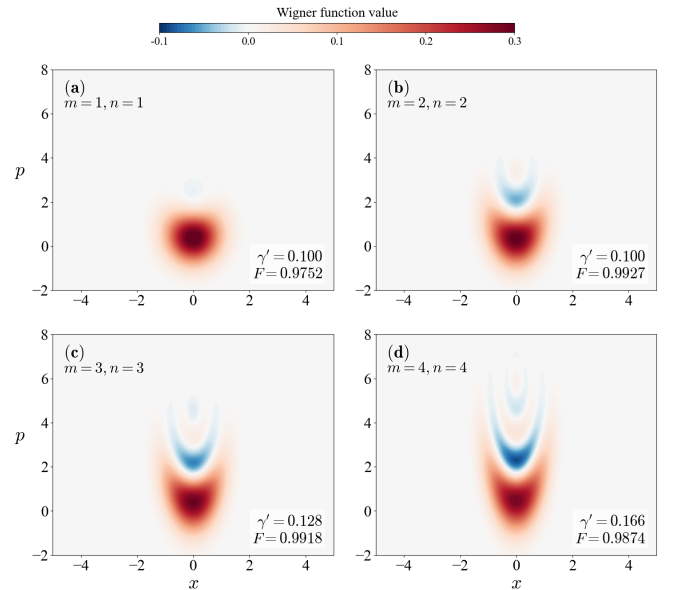


Figure 3. Wigner functions of the optimized output states for catalytic configurations  $m = n = 1, 2, 3, 4$  with coherent input, showing cubic-phase-state features.

Fig. 3, where the characteristic non-Gaussian features—negative regions and asymmetric distortions—are clearly visible and closely match those of the ideal cubic phase states. For comparison, Fig. 4 shows the Wigner functions for several non-catalytic configurations, including (1, 4), (1, 5), and (2, 5), and the reference case (0, 4), illustrating the rich variety of non-Gaussian states accessible within our framework.

A key observation from Table I is that the optimal OPA gain  $g$  increases with the catalysis order. This trend reflects the fact that higher-order catalysis requires stronger nonlinear interactions to generate the higher-Fock components necessary for the cubic phase state. The optimal input coherent amplitude  $\alpha$  (fifth column) is purely imaginary for all configurations. Since the imaginary part of  $\alpha$  determines the displacement along the  $p$ -quadrature (momentum), a negative imaginary amplitude shifts the Wigner function toward the negative  $p$  direction. This initial displacement, combined with sub-

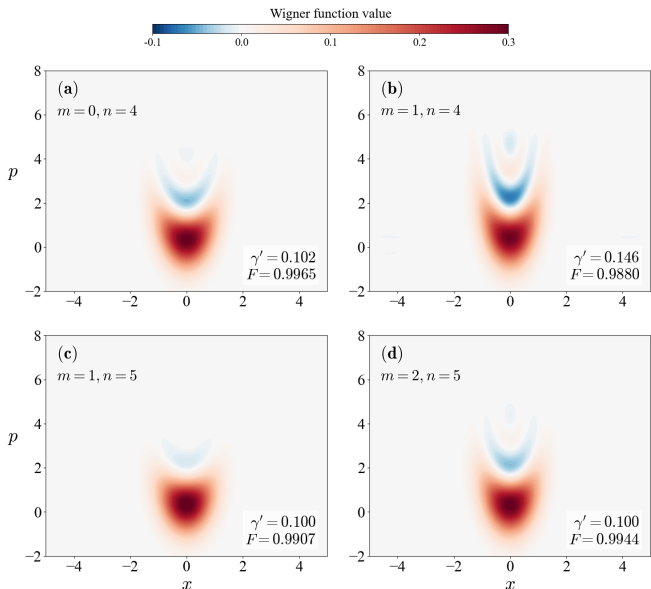


Figure 4. Wigner functions for non-catalytic configurations (1,4), (1,5), (2,5) and the reference case (0,4) with coherent input, optimized to generate high-fidelity cubic phase states.

sequent Gaussian corrections, allows the state to be positioned in phase space to match the target cubic phase state.

The Gaussian correction parameters—the real squeezing parameter  $r_{corr}$  (sixth column) and the complex displacement  $\beta_{corr}$  (seventh column) take values where  $r_{corr}$  is positive and  $\beta_{corr}$  is purely imaginary for all configurations. The positive imaginary part of  $\beta_{corr}$  shifts the Wigner function in the positive  $p$  compensating for the negative  $p$ -displacement introduced by the initial  $\alpha$ . Notably,  $r_{corr}$  increases with the catalysis order, from 0.203 for (1,1) to 0.647 for (4,4), indicating that higher-order catalysis produces states that require stronger squeezing correction to match the target. We note that implementing the corrective squeezing on a displaced non-Gaussian state is experimentally demanding; nevertheless, it has been demonstrated in Ref. [41] and is becoming increasingly feasible with modern homodyne feedback techniques. The fact that both  $\alpha$  and  $\beta_{corr}$  are purely imaginary means that all displacements occur exclusively along the  $p$ -quadrature, while the  $x$ -quadrature remains unaffected—a specific phase-space alignment strategy that, together with the positive squeezing correction, enables high-fidelity conversion to the cubic phase state. The Wigner functions in Figs. 3 and 4 all exhibit reflection symmetry about the  $x$ -axis, i.e.,  $W(x, p) = W(x, -p)$ . This symmetry follows directly from the fact that both the input displacement  $\alpha$  and the correction displacement  $\beta_{corr}$  are purely imaginary, so all displacements occur exclusively along the  $p$ -quadrature, leaving the  $x$ -axis symmetry intact. Importantly, this symmetry matches that of the ideal cubic phase state, confirming that our phase-space alignment

strategy successfully reproduces the correct symmetry structure of the target state.

The success probabilities  $P_{trial}$  (last column) vary widely across configurations. The reference (0,4) case offers the highest value, on the order of  $10^{-2}$ . For catalytic configurations range,  $P_{trial}$  ranges from  $10^{-2}$  for (1,1) down to  $10^{-7}$  for (4,4), reflecting the increasing experimental difficulty of preparing higher-order Fock states and detecting higher photon numbers. Non-catalytic configurations such as (1,4), (1,5), and (2,5) provide intermediate probabilities on their order of  $10^{-3}$  to  $10^{-4}$ , offering useful trade-offs between fidelity and generation rate. As discussed in Sec. II, these low probabilities can be overcome by operating at high repetition rates, making all configurations experimentally feasible.

In summary, our OPA heralding framework provides a versatile platform for generating high-fidelity ( $> 0.99$ ) cubic phase states from coherent light across a broad range of  $(m, n)$  configurations. Compared with the deterministic Gaussian conversion protocol of Zheng et al. [14], which requires a complex trisqueezed state as a non-Gaussian seed, our scheme uses only low-order Fock states (typically  $|1\rangle$  or  $|2\rangle$ ), which are significantly easier to prepare, while achieving comparable or higher fidelities. Compared with the vacuum-input OPA scheme of Erkilic et al. [34] ( $m = 0$ ), which is restricted to vacuum idler input, our work generalises the framework to arbitrary Fock-state inputs and identifies the catalytic condition  $m = n$  as a new route to high-fidelity cubic phase states with the added advantages of parity preservation and idler restoration. The catalytic configurations offer these unique features at the cost of lower success probabilities for higher orders, while non-catalytic configurations provide intermediate trade-offs. This flexibility allows experimentalists to choose the optimal configuration balancing fidelity, success probability, and resource requirements for their specific tasks.

#### IV. AMPLIFIED CAT STATES

We now turn to the second application of our OPA heralding framework: the amplification of Schrodinger cat states. Specifically, we consider an input cat state  $|Cat\rangle_{\alpha, \theta}$  in the signal port, with  $\theta = 0$  for an even cat state (ECS) and  $\theta = \pi$  for an odd cat state (OCS), and investigate how the heralding process transforms it under various  $(m, n)$  configurations.

Substituting the cat state input into the general heralded state of Eq. (3) and using the identity  $e^{-a^\dagger a} |Cat\rangle_{\alpha, \theta} \propto |Cat\rangle_{\alpha/g, \theta}$ , we obtain the unnormalised output state

$$|\Psi\rangle_{cat, m, n} = \sum_{k=0}^m C'_k |Cat, n - m + k\rangle_{\alpha/g, \theta + \pi k}, \quad (14)$$

where we have used  $a^k|Cat\rangle_{\alpha/g,\theta} = (\alpha/g)^k|Cat\rangle_{\alpha/g,\theta+\pi k}$ ,

$$C'_k = \exp\left[-\frac{G^2|\alpha|^2}{2}\right] \mathcal{N}_{n-m+k}^{-1} H(k, m, n) \alpha^k$$

and

$$|Cat, l\rangle_{\alpha,\theta} = \mathcal{N}_l (a^\dagger)^l |Cat\rangle_{\alpha,\theta} \quad (15)$$

is the  $l$ -photon-added cat state with normalization

$$\mathcal{N}_l = (2l)! \left[ L_l(-|\alpha|^2) + L_l(|\alpha|^2) e^{-2|\alpha|^2} \cos(\theta + \pi l) \right]^{-1/2}, \quad (16)$$

with  $L_l(x)$  is the Laguerre polynomial of order  $l$ . This representation reveals that the heralded state is a superposition of  $m+1$  terms, each corresponding to the input cat state with a different number of added photons and a phase shift  $\pi k$  acquired by the relative phase between the two coherent components.

A key property of this transformation is the parity selection rule. The parity of the heralded output state is determined by the parity of the input cat state multiplied by the factor  $(-1)^{m+n}$ . Specifically, for an even cat input ( $\theta = 0$ ), the output parity is  $(-1)^{m+n}$ ; for an odd cat input ( $\theta = \pi$ ), the output parity is  $(-1)^{m+n+1}$ .

When the catalytic condition  $m = n$  is imposed, the expression simplifies considerably:

$$|\Psi'\rangle_{cat,n,n} = \sum_{k=0}^n C''_k |Cat, k\rangle_{\alpha/g,\theta+\pi k}, \quad (17)$$

where  $C''_k = \exp\left[-\frac{G^2|\alpha|^2}{2}\right] \mathcal{N}_k^{-1} H(k, n, n) \alpha^k$ . Under this condition, the parity of the input cat state is strictly preserved: an even cat input yields an even cat output, and an odd cat input yields an odd cat output. This parity preservation is a distinct feature of our catalysis protocol. In previous cat-state amplification schemes, such as the homodyne-based breeding protocol of Sychev et al. [42], an odd cat state is converted into an even cat state—i.e., the parity is flipped. By contrast, our OPA catalysis scheme preserves the parity of the input cat state, offering a new degree of control in cat-state engineering.

In this work, we primarily investigate the similarity between our heralded output states and the ideal squeezed Schrodinger cat states (SOSC for odd, SESC for even), defined as

$$|\Psi_\theta\rangle = \mathcal{N}_\theta S(\gamma) |Cat\rangle_{\alpha,\theta}, \quad (18)$$

where the normalization coefficient is given by  $\mathcal{N}_\theta = (2 + 2e^{-2\alpha^2} e^{2\gamma} \cos\theta)^{-1/2}$ , and squeezing parameter  $\gamma$  to be real. The fidelity between our heralded state and this target is then maximised over the parameters  $(g, \alpha_{in}, \alpha_{out}, \gamma)$ , where  $\alpha_{in}$  is the input cat amplitude,  $\alpha_{out}$  is the target amplitude, and  $g$  and  $\gamma$  are the OPA gain and target squeezing, respectively.

## A. Odd cat state input

We first consider an odd cat state input ( $\theta = \pi$ ). In order to check general feature of output signal state corresponding to the OCS input, we plot the Wigner functions of the heralded output states for configurations  $m, n = 0, 1, 2, 3, 4$  while fixing  $g = 1.5$  and  $\alpha_{in} = 1.0$  and results shown in Fig. 5. It can observe that the output state for every configuration possesses  $(-1)^{n+m+1}$  parity and have significant interference fringes characterized by pronounced Wigner negativity. We also noticed that some configuration still very similar to ideal squeezed cat sates. To check this point, in this subsection we mainly focus on catalytic configuration  $m = n$ , where the output state retains the same parity as the input cat state.

For the vacuum-idler case  $m = n = 0$ , the output is simply an attenuated odd cat state with reduced amplitude  $\alpha/g$ , as expected from the noiseless attenuation discussed in Sec. III. By optimising the overlap between  $|\Psi'\rangle_{cat,n,n}$  ( $\theta = \pi$ ) and the target SOSC state  $|\Psi_\pi\rangle$  we find that as the catalysis order increases, the Wigner functions develop richer structures—negative regions become more pronounced, and the two positive peaks move farther apart along the  $x$ -axis (see Fig. 6). These plots display the characteristic features of SOSCs: a deep negative dip at the origin, two well-separated positive peaks, and reflection symmetry about both axes. The high similarity to the ideal SOSC targets is visually evident. Furthermore, for input odd cat amplitudes  $\alpha_{in} \lesssim 1.3$ , our catalytic protocol can amplify them to large-amplitude SOSCs with  $\alpha_{out} \geq 2.0$  while maintaining extremely high fidelity ( $> 0.99$ ).

Figure 7 (a) shows the optimized fidelity of  $|\Psi'\rangle_{cat,n,n}$  ( $\theta = \pi$ ) to the target SOSC state  $|\Psi_\pi\rangle$  as a function of  $\alpha_{in}$  for  $n = m = 1, 2, 3, 4$ , while Fig. 7 (b) displays the corresponding amplification ratio  $\eta = \alpha_{out}/\alpha_{in}$ . From Fig. 7 (a), we observe that for each catalytic configuration  $(n, n)$ , the fidelity exceeds 0.99 over a finite window of input amplitudes  $\alpha_{in}$  for a specific optimized OPA gain  $g$ . Specifically, for (1, 1) this high-fidelity region covers  $\alpha_{in} \lesssim 1.1$ ; for (2, 2), it extends to  $\alpha_{in} \lesssim 1.43$ ; for (3, 3), the region is around  $\alpha_{in} \lesssim 0.93$ ; and for (4, 4), it spans  $\alpha_{in} \lesssim 1.48$ . Within these regions, the amplification ratio is always greater than unity, ranging from approximately  $1.52 \leq \eta \leq 2.3$ . Correspondingly, within these high-fidelity regions the output amplitude reaches values of approximately  $\alpha_{out} \lesssim 2.08$  for (1,1),  $\alpha_{out} \lesssim 2.30$  for (2, 2),  $\alpha_{out} \lesssim 2.09$  for (3, 3), and  $\alpha_{out} \lesssim 2.61$  for (4, 4) [see Fig. 7 (b)]. Notably, for  $\alpha_{in} \lesssim 1.1$ , the amplification ratio  $\eta$  ranges from about 1.52 to 2.3, ensuring that the output consistently falls into the large-amplitude regime  $\alpha_{out} \geq 2$  in a single successful trial for the specific configurations. Concrete examples are listed in Table II. For instance, with the simplest catalytic configuration (1,1), an input OCS with amplitude  $\alpha_{in} = 1.06$ , readily preparable by single-photon subtraction, is transformed into a large-amplitude squeezed cat state with  $\alpha_{out} = 2.02$  at a fidelity of 0.992 and a single-trial success probability

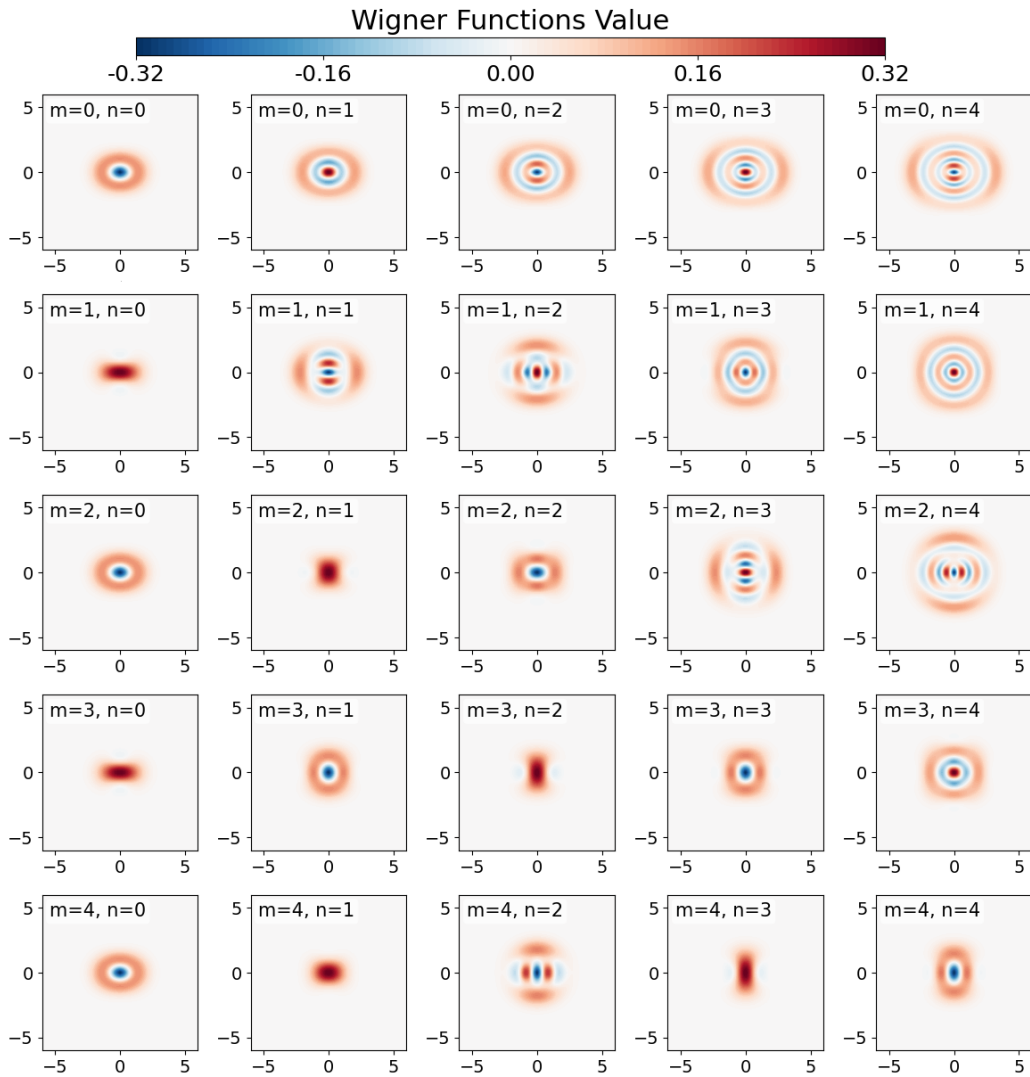


Figure 5. Wigner functions of the heralded output states for odd cat state (OCS) input for various  $(m, n)$  configurations with  $g = 1.5$  and  $\alpha_{in} = 1.0$ . The parity of these output states is determined by  $(-1)^{n+m+1}$ .

of 0.27%. This performance compares favourably with previous cat-state amplification schemes.

Remarkably, the input amplitude  $\alpha_{in} = 1.06$  sits at the upper boundary of the high-fidelity regime ( $\alpha \lesssim 1.2$ ) for the standard single-photon-subtracted squeezed vacuum state, which is known to produce odd kitten states with fidelity above 0.99 [21, 43]. Our  $(1, 1)$  catalytic configuration takes this same type of state and amplifies it continuously into the large-amplitude regime  $\alpha_{out} \geq 2.0$  while maintaining comparable fidelity—a task that conventional photon subtraction alone cannot achieve. This demonstrates that our protocol is not merely a state converter but a genuine amplifier of non-Gaussian quantum resources, capable of bridging the gap between easily producible small-amplitude cat states and the large-amplitude states required for fault-tolerant quantum error correction [44].

## B. Even cat state input

We now consider an even cat state input ( $\theta = 0$ ). The Wigner functions of the heralded output states for configurations  $n, m = 0, 1, 2, 3, 4$  are shown in Fig. 8. The parity of output state decided by  $(-1)^{n+m}$  and this rule can be seen from the Wigner function profiles present in Fig. 8. For catalytic configurations  $n = m = 1, 2, 3, \dots$ , unlike the OCS case, ECSs have a positive central peak at the origin and negative regions at larger phase-space radii. As the catalysis order increases, the Wigner functions develop more complex interference patterns, with additional negative regions emerging.

Figure 9 shows the optimised fidelity between the heralded output state and the ideal SESC state for catalytic configurations  $m = n = 2, 3, 4$  as a function of the input amplitude  $\alpha_{in}$ . For each configuration, the curves are obtained by optimising over all parameters and selecting

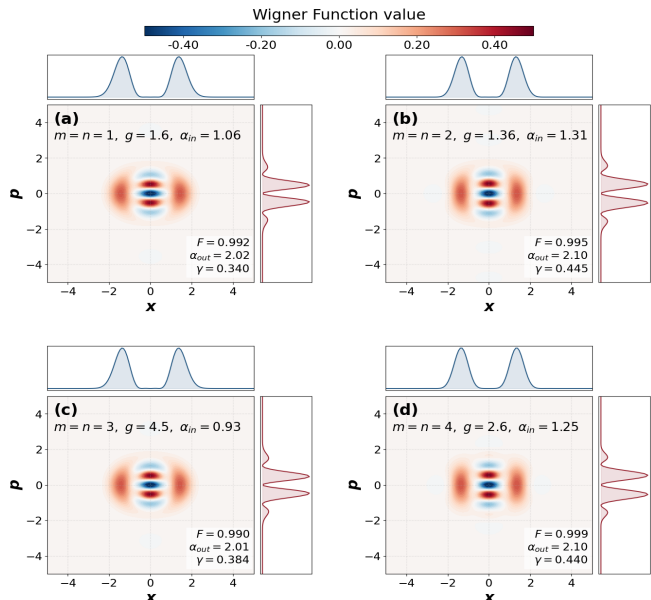


Figure 6. Wigner functions of the optimized output states for catalytic configurations  $m = n = 1, 2, 3, 4$  with odd cat state (OCS) input, showing amplified squeezed odd cat state features. In all cases the fidelity exceeds  $F > 0.99$ .

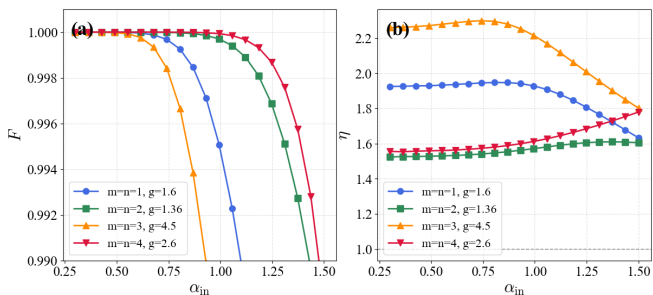


Figure 7. (a) Optimal fidelity between the output state  $|\Psi\rangle_{cat,n,n}$  and the target state  $|\Psi_\theta\rangle$  as a function of coherent amplitude of input odd cat state (OCS) for  $m = n = 1, 2, 3, 4$ . (b) Corresponding amplification ratio  $\eta = \alpha_{out}/\alpha_{in}$  that maximizes the fidelity in (a).

the OPA gain  $g$  that yields the highest fidelity across the entire range of input amplitudes considered. The fidelity remains above 0.98 for all configurations over a broad range of input amplitudes, with many cases achieving near-unity fidelity ( $F \geq 0.999$ ).

For the ECS input, the high-fidelity windows  $F \geq 0.99$  regions are notably broad: (2, 2) covers  $\alpha_{in} \lesssim 1.53$ , (3, 3) extends to  $\alpha_{in} \lesssim 1.42$ , and (4, 4) spans  $\alpha_{in} \lesssim 1.43$ . Within these regions, the output amplitude reaches  $\alpha_{out} \lesssim 2.47, 2.50$ , and  $2.46$ , respectively, corresponding to a moderate amplification ratio of  $1.45 \leq \eta \leq 1.8$ . Correspondingly, within these high-fidelity regions the output amplitude reaches values of approximately  $\alpha_{out} \lesssim 2.47$  for (2, 2),  $\alpha_{out} \lesssim 2.50$  for (3, 3), and  $\alpha_{out} \lesssim 2.46$  for (4, 4).

Table II. Optimized parameters for odd cat state (OCS) amplification under catalytic configurations  $m = n = 1, 2, 3, 4$ . For each configuration, we list the OPA gain  $g$ , the amplitude  $\alpha_{in}$ , the target state characteristics ( $\alpha_{out}$ , squeezing  $\gamma$ ), the success probability  $P_{trial}$ , and the optimized fidelity  $F$ .

$(m, n)$	$g$	$\alpha_{in}$	Target state		$F$	$P_{trial}$
			$\alpha_{out}$	$\gamma$		
(1, 1)	1.6	0.30	0.58	0.03	1.000	$1.39 \times 10^{-3}$
		1.06	2.02	0.34	0.992	$2.73 \times 10^{-3}$
		1.31	2.31	0.39	0.976	$3.94 \times 10^{-3}$
(2, 2)	1.36	0.30	0.46	0.03	1.000	$2.78 \times 10^{-4}$
		1.06	1.67	0.31	0.999	$3.33 \times 10^{-4}$
		1.31	2.11	0.45	0.995	$3.71 \times 10^{-4}$
(3, 3)	4.5	0.30	0.68	0.05	1.000	$5.73 \times 10^{-7}$
		1.06	2.30	0.43	0.980	$1.66 \times 10^{-6}$
		1.31	2.56	0.47	0.958	$2.64 \times 10^{-6}$
(4, 4)	2.6	0.30	0.47	0.03	1.000	$2.74 \times 10^{-7}$
		1.06	1.72	0.32	0.999	$3.41 \times 10^{-7}$
		1.31	2.24	0.48	0.998	$3.94 \times 10^{-7}$

Table III. Optimized parameters ( $g, \alpha_{in}$ , target state  $\{\alpha_{out}, \gamma\}$ ,  $P_{trial}$  and  $F$ ) for even cat state (ECS) amplification under catalytic configurations

$(m, n)$	$g$	$\alpha_{in}$	Target state		$F$	$P_{trial}$
			$\alpha_{out}$	$\gamma$		
(1, 1)	1.1	0.50	0.37	0.015	1.000	$4.91 \times 10^{-2}$
		1.00	0.74	0.061	1.000	$3.64 \times 10^{-2}$
		1.50	1.13	0.149	0.997	$1.67 \times 10^{-2}$
(2, 2)	2.8	0.50	0.85	0.070	1.000	$1.62 \times 10^{-5}$
		1.00	1.71	0.246	0.999	$4.43 \times 10^{-5}$
		1.50	2.43	0.397	0.991	$9.49 \times 10^{-5}$
(3, 3)	1.93	0.50	0.73	0.016	1.000	$3.33 \times 10^{-6}$
		1.00	1.51	0.262	0.999	$5.70 \times 10^{-6}$
		1.50	2.70	0.661	0.981	$8.60 \times 10^{-6}$
(4, 4)	1.65	0.50	0.74	0.076	1.000	$3.85 \times 10^{-7}$
		1.00	1.53	0.309	0.999	$6.41 \times 10^{-7}$
		1.50	2.63	0.688	0.984	$8.84 \times 10^{-7}$

In Table III lists the optimised parameters and resulting fidelities for catalytic configurations  $m = n = 1, 2, 3, 4$ , using the same parameter structure as Table II. Our protocol indeed provides an extremely good approximation to the target SESC state when the input is an even cat state. For (2, 2) and (4, 4) with  $\alpha_{in} = 1.0$ , the output reaches  $\alpha_{out} = 1.71$  and  $1.53$  with same fidelity  $F = 0.999$ . The corresponding success probabilities range from  $10^{-5}$  down to  $10^{-7}$ , consistent with the trends observed for the odd cat case.

To further confirm our claim, we present in Fig. 10 the Wigner functions of the output states for catalytic configurations (2, 2), (3, 3) and (4, 4), corresponding to an ECS input with amplitude  $\alpha_{in} = 1.35$ . All three configurations produce excellent approximations to the target SESC states, with amplified coherent amplitudes  $\alpha_{out} = 2.23, 2.30$ , and  $2.25$ , respectively, while maintaining exceptionally high fidelity  $F = 0.995$ . The corresponding success probabilities are on the order of  $10^{-5}$

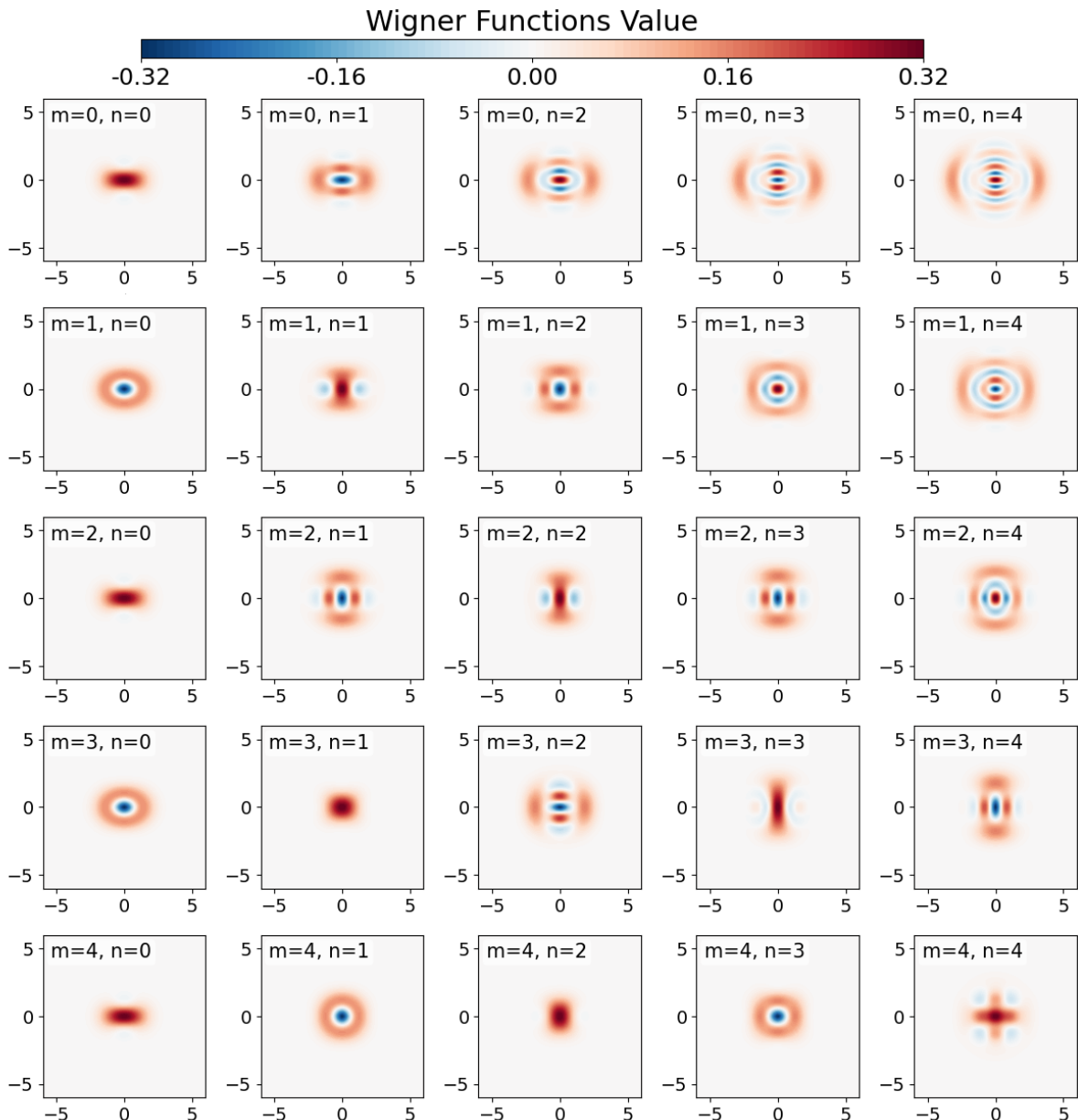


Figure 8. Wigner functions of the heralded output states for even cat state (ECS) input for various  $(m, n)$  configurations. with  $g = 1.5$  and  $\alpha_{in} = 1.0$ . The parity of these output states is determined by  $(-1)^{n+m}$ .

for  $(2, 2)$  to  $10^{-7}$  for  $(3, 3)$  and  $(4, 4)$ . These Wigner plots provide direct visual evidence that our protocol reliably generates large-amplitude squeezed cat states with high fidelity across different catalysis orders.

We note an interesting contrast with the OCS case. For ECS inputs, the  $(1, 1)$  configuration does not amplify the state but instead acts as a noiseless attenuator, yet its performance remains remarkably good—for example, reducing  $\alpha_{in} = 1.0$  to  $\alpha_{out} = 0.74$  with fidelity  $F = 1.000$  [see Table III]. This attenuation behavior is also evident in Fig. 9 (b), where the amplification ratio  $\eta = \alpha_{out}/\alpha_{in}$  remains below unity across the entire range of  $\alpha_{in}$  considered.

To confirm that this is indeed attenuation rather than amplification, we have scanned the full range of allowed OPA gain  $g$  for the  $(1, 1)$  configuration with ECS inputs. The fidelity to the target SESC state remains low for all values of  $g$  except in the specific parameter regime corresponding to the noiseless attenuation regime. This confirms that the  $(1, 1)$  catalysis acts as a genuine attenuator for even cat inputs, in stark contrast to its amplifying behavior for odd cat inputs.

A plausible explanation for this parity-dependent behavior lies in the explicit form of the  $(1, 1)$  heralded state, which contains a term proportional to  $a^\dagger a g^{-a^\dagger a}$ . For an ECS input, the operator  $a^\dagger a$  removes the vacuum compo-

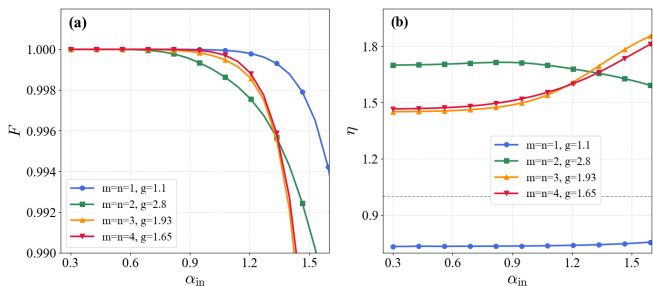


Figure 9. (a) Optimized fidelity between the heralded output state and the ideal squeezed even cat state as a function of the input amplitude  $\alpha_{in}$  for catalytic configurations  $m = n = 1, 2, 3, 4$ . (b) Corresponding amplification ratio  $\eta = \alpha_{out}/\alpha_{in}$  that maximizes the fidelity in (a).

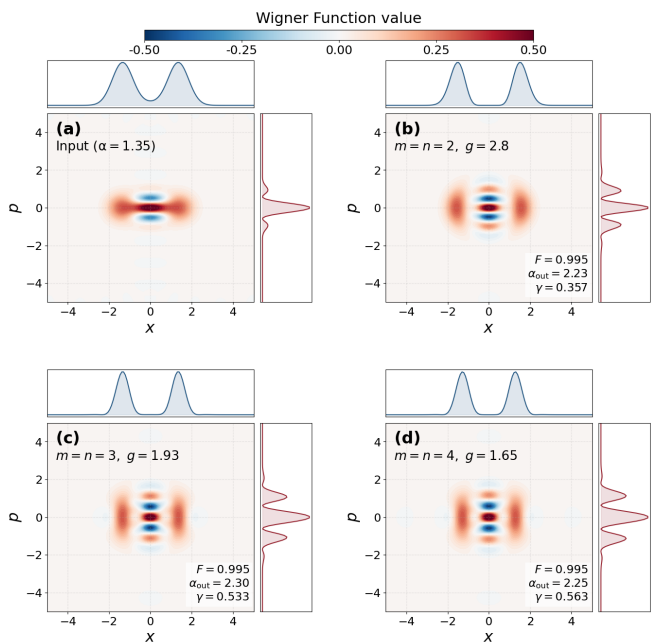


Figure 10. Wigner functions of the optimized output states for catalytic configurations  $m = n = 2, 3, 4$  with even cat state (ECS) input, showing amplified squeezed even cat state features with  $F = 0.995$ .

ment of the state, reducing the relative weight of low-lying Fock components and effectively shrinking the separation between the two coherent peaks rather than amplifying it. For an odd cat input, which has no vacuum component, the same operator leads to amplitude amplification. This provides a clear physical picture of why the (1,1) catalysis attenuates ECS while amplifying OCS.

### C. Non-catalytic configurations

In addition to the catalytic cases, we have also investigated non-catalytic configurations ( $m \neq n$ ) for cat state amplification. Here, the parity of our approximated cat

states are not preserved, and determined by  $(-1)^{m+n}$  and  $(-1)^{m+n+1}$  for ECS and OCS inputs, respectively.

Figure 11 shows the optimized fidelity as a function of the input amplitude  $\alpha_{in}$  for several non-catalytic configurations, including (0, 2), (1, 2), (1, 3) and (3, 2) for ECS inputs (Fig. 11 (a) and (b)), and (0, 2), (1, 2), (3, 2) and (4, 2) for OCS inputs (Fig. 11 (c) and (d)). For each configuration, the OPA gain  $g$  is optimised to maintain high fidelity across the considered range of input amplitudes. For both inputs, the amplification ratio  $\eta = \alpha_{out}/\alpha_{in}$  is consistently greater than unity, ensuring that the output falls into the large-amplitude regime for appropriate input parameters [see Fig. 11 (b) and (d)].

Table IV presents the optimized parameters and fidelities for representative non-catalytic configurations. For ECS inputs, the (1,3) configuration achieves a fidelity of 0.991 with  $\alpha_{out} = 3.45$  and  $\gamma = 0.26$ , at a success probability of  $1.13 \times 10^{-3}$ . The reference (0, 2) configuration—previously studied in the context of photon addition [32]—achieves a comparable fidelity of 0.991 with a similar output amplitude and success probability. The catalytic configurations (2, 2), (3, 3) and (4, 4) from Table III achieves comparable fidelity but with a lower success probability. This illustrates the trade-off between catalytic advantages (parity preservation, idler restoration) and generation rate.

For OCS inputs, the non-catalytic configurations exhibit distinct trade-offs. The (1, 2) configuration achieves a fidelity of 0.991 with a practical success probability of  $2.2 \times 10^{-2}$ , amplifying  $\alpha_{in} = 1.97$  to  $\alpha_{out} = 2.69$ . While the (3, 2) configuration marginally improve the fidelity to 0.993, amplifying  $\alpha_{in} = 1.76$  to  $\alpha_{out} = 2.31$ . This comes at a prohibitive cost—the success probability plummets to  $5.52 \times 10^{-6}$  (a four-orders-of-magnitude reduction), rendering it experimentally inefficient for most purposes. Interestingly, the reference (0, 2) configuration yields the largest output amplitude among the three which amplifying  $\alpha_{in} = 1.97$  to  $\alpha_{out} = 3.46$  with a moderate success probability of  $4.59 \times 10^{-3}$  and a fidelity of 0.991. This highlights that the (0, 2) scheme serves as an "amplitude-maximizing" amplifier, whereas the (1, 2) case provides the best overall balance between fidelity, rate, and operable bandwidth. Collectively, these results demonstrate that non-catalytic configurations offer flexible trade-offs—achieving comparable or even superior performance for specific targets at the expense of losing the parity preservation and idler restoration unique to the catalytic case.

Remarkably, the (1, 2) non-catalytic configuration with ECS inputs stands out as one of the best-performing cases in our entire protocol. Over a wide input range  $\alpha_{in} \in [0.5, 2.5]$ , the fidelity to the target SOS state consistently exceeds 0.992, while the amplification ratio ranges from  $\eta \approx 1.78$  at small amplitudes to  $\eta \approx 1.23$  at larger ones, and the success probability remains between 1.2% and 2.2% [see Fig. 11 (a) and (b)]. For example, with the (1, 2) non-catalytic configuration, an ECS input of amplitude  $\alpha_{in} = 1.18$  is transformed into

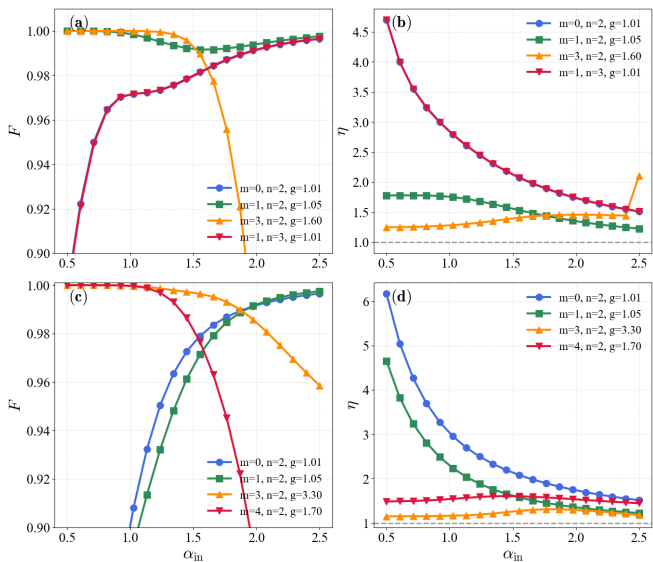


Figure 11. Optimized fidelity (left column) and amplification ratio (right column) for non-catalytic configurations ( $m \neq n$ ): (a,b) for even cat state (ECS) inputs with configurations (0, 2), (1, 2), (1, 3) and (3, 2); (c,d) for odd cat inputs with configurations (0, 2), (1, 2), (3, 2) and (4, 2).

a target SOSC state with amplitude  $\alpha_{out} = 2.02$  and squeezing  $\gamma = 0.23$ , while maintaining a high fidelity of 0.996 and a success probability of 1.74% [see Table IV]. This means that small even kittens can be amplified to large-amplitude squeezed odd cat states with near-perfect fidelity across a broad parameter regime. To the best of our knowledge, such high-fidelity amplification of even cat states to odd cat states—accompanied by a parity flip—has not been reported in previous cat-state amplification schemes. This parity-flipping amplification capability, combined with the parity-preserving catalysis demonstrated earlier, establishes our OPA platform as a versatile tool for controlled cat-state engineering with tunable parity outcomes.

#### D. Discussion of amplification performance

Our protocol amplifies input cat states to large-amplitude squeezed cat states with high fidelity ( $F \geq 0.99$ ) and success probabilities ranging from  $10^{-2}$  to  $10^{-7}$  across various catalytic and non-catalytic configurations. Even-cat inputs yield higher fidelities than odd-cat inputs for the same catalysis order, particularly at small amplitudes, but exhibit less pronounced amplification ( $\alpha_{out}/\alpha_{in}$ ). This trade-off reflects the larger vacuum component of even cat states, which improves target-state overlap but limits amplitude gain.

To generate large-amplitude cat states, numerous theoretical and experimental schemes have been proposed, including photon subtraction [32, 34, 42, 45–48] and photon catalysis [49] and postselected measurement [50, 51]

schemes were conducted. However, many of these approaches face significant experimental overhead. Multi-photon (three-photon) subtraction schemes produce amplitudes  $\alpha \approx 1.6$ -1.7 with success probability  $\sim 10^{-9}$  [35, 52], while Song et al. [47] predict  $\alpha_{out} \approx 2.51$  with success probability  $\sim 10^{-7}$ . The homodyne breeding protocol of Sychev et al. [42] achieves  $\alpha_{out} \approx 1.85$  with success probability  $10^{-8}$  via two-photon detection with additional homodyne conditioning. More recently, Erkilic et al. [34] demonstrated an OPA-based scheme that generates large-amplitude squeezed cat states ( $\alpha \approx 4.9 - 5.7$ ,  $F \approx 0.99$ ) using only Gaussian inputs (squeezed vacuum) and low per-round photon detection (2-3 photons), but requires 5–6 iterative rounds with an optical switch, leading to cumulative photon detections of 12–15 photons and overall success probabilities of  $10^{-4} - 10^{-6}$ , limited by switching loss. While their approach eliminates the need for non-Gaussian seed states, the iterative nature introduces experimental complexity and loss accumulation.

For high-success-rate generation, schemes based on two squeezed-state inputs interfering on a beam splitter with heralded photon detection have been proposed. Luo and Mahmoodian [53] achieve  $F \geq 0.99$ ,  $\alpha_{out} > 2$ , and success probabilities  $\sim 0.5$  with single-photon detection, but require strong squeezing and a dual-input interferometric setup with stringent phase synchronization and additional non-Gaussian resource preparation. The generalized photon subtraction (GPS) scheme [48] generates  $\alpha_{out} = \sqrt{10} \approx 3.16$  with  $F \approx 0.997$  via 10-photon detection, yet demands extreme squeezing and high-order photon-number resolution.

Our OPA-based protocol achieves output amplitudes comparable to those of previous schemes, but with a different experimental cost structure. As shown in Table II-IV, the generated states exhibit  $\alpha_{out} \geq 2.0$ , proper squeezing, and  $F \geq 0.99$ . Notably, the (0, 2) and (1, 3) configurations—requiring only 2- or 3- photon detection in a single pass—yield  $\alpha_{out} \approx 3.46$ ,  $F = 0.991$ , and success probability on the order of  $10^{-3}$ . These amplitudes and fidelities are comparable to GPS and Erkilic’s schemes, while operating at 100 MHz also enables Mcps-level generation rates.

The cost of the present scheme is that for some configurations it requires a seed cat state with larger amplitude, such as  $\alpha_{in} \approx 1.97$ . However, such seed states are readily producible with current laboratory technology using various established methods [18, 50, 51, 54], and the gain operations used in this work are experimentally undemanding. Critically, 1-3 photon detection is experimentally mature, with PNRD efficiency approaching unity at low photon numbers. In contrast, iterative schemes and high-photon-number (e.g., 10-photon) resolution suffer from cumulative loss, synchronization overhead, and significant efficiency degradation.

Importantly, the amplified cat states produced by our protocol can themselves serve as seeds for subsequent amplification rounds. For example, a small-amplitude cat state ( $\alpha_{in} \approx 1$ )—readily generated by standard single-

Table IV. Optimized parameters ( $g$ ,  $\alpha_{in}$ , target state  $\{\alpha_{out}, \gamma$ , parity $\}$ ,  $P_{trial}$  and  $F$ ) for cat state amplification under non-catalytic configurations ( $m \neq n$ ), for both even cat state (ECS) and odd cat state (OCS) inputs.

Input	$(m, n)$	$g$	$\alpha_{in}$	Target state			$F$	$P_{trial}$
				$\alpha_{out}$	$\gamma$	Parity		
ECS	(1, 2)	1.05	1.18	2.02	0.23	Odd	0.996	$1.74 \times 10^{-2}$
	(1, 3)	1.01	1.97	3.45	0.26	Even	0.991	$1.13 \times 10^{-3}$
	(0, 2)	1.01	1.97	3.46	0.26	Even	0.991	$4.59 \times 10^{-3}$
	(3, 2)	1.60	1.45	2.00	0.49	Odd	0.996	$1.34 \times 10^{-5}$
OCS	(1, 2)	1.05	1.97	2.69	0.20	Even	0.991	$2.20 \times 10^{-2}$
	(0, 2)	1.01	1.97	3.46	0.25	Odd	0.991	$4.59 \times 10^{-3}$
	(3, 2)	3.30	1.76	2.31	0.35	Even	0.993	$5.52 \times 10^{-6}$
	(4, 2)	1.70	1.34	2.15	0.51	Odd	0.993	$2.59 \times 10^{-7}$

photon subtraction—can be amplified via the (1,1) catalytic configuration to  $\alpha_{out} \approx 2.0$ . We note that a squeezed odd cat state with  $\alpha_{out} \approx 2$  and  $F = 0.992$  can also be generated from a squeezed vacuum input using the (1, 2) configuration [18]. These outputs can then be fed into a second amplification round using, for instance, the (1,2) non-catalytic configuration, yielding  $\alpha_{out} \approx 3.46$ . Assuming a one-time seed preparation success probability of  $\sim 10^{-2}$  and a single-round OPA heralding probability of  $\sim 10^{-3}$ , the total success probability for two rounds is on the order of  $10^{-5}$  to  $10^{-6}$ . This is comparable to that of iterative OPA schemes [34] and higher than multi-photon subtraction schemes [47, 48], yet our protocol avoids the need for extreme squeezing, high-order photon detection, or optical switching.

This approach thus offers a flexible and complementary route to large-amplitude squeezed cat states, using moderate resources instead of extreme squeezing, high-order detection, or iterative breeding. By selecting the appropriate catalytic or non-catalytic configuration, the protocol can be tailored to suit specific application needs while maintaining high generation rates suitable for fault-tolerant quantum computing [4, 20, 55, 56].

## V. PHOTON LOSS

Since the squeezing operation can reduce the average photon number of cat states, the squeezed cat states survive longer than usual cat states in a lossy environment. To evaluate the practical feasibility of our protocol, we model photon loss using the Lindblad master equation

$$\frac{d\rho(t)}{dt} = \kappa (2a\rho(t)a^\dagger - a^\dagger a\rho(t) - \rho(t)a^\dagger a), \quad (19)$$

where  $\kappa$  the photon loss and  $a$  ( $a^\dagger$ ) is the annihilation (creation) operator of the signal mode. This master equation is equivalent to coupling the signal mode to a vacuum environment through a fictitious beam splitter with transmissivity  $e^{-\kappa t}$ , where  $t$  is the interaction time. The solution to Eq. (19) maps the initial state  $\rho_0$  to the lossy state  $\rho_\kappa = \mathcal{L}_\kappa(\rho_0)$ , with the average photon number scaling as  $\langle n \rangle \rightarrow e^{-\kappa t} \langle n \rangle$ .

In this section we also illustrate the effects of photon loss on the negativity and complexity of our heralded states. The Wigner negativity of a quantum state  $\rho$  is defined as [57]

$$\mathcal{N} = \int_{\mathbb{C}} |W(\alpha|\rho)| \frac{d^2\alpha}{\pi} - 1, \quad (20)$$

where  $W(\alpha|\rho)$  is the Wigner function of the state  $\rho$ . This quantity characterizes the volume of the negative part of the Wigner function in phase space. It serves as a strong indicator of non-classicality: a non-zero value of  $\mathcal{N}$  signals genuine quantum interference. However, Wigner negativity does not very accurately capture structural features such as squeezing or high photon number when the Wigner function remains non-negative (e.g., for SV states).

In contrast, the complexity  $\mathcal{C}(\rho)$  introduced by Tang et al. [58] is defined via the always-positive Husimi function  $Q(\alpha|\rho) = \langle \alpha|\rho|\alpha \rangle$ :

$$\mathcal{C}(\rho) = e^{S_W(\rho)-1} I(\rho) \quad (21)$$

with the Wehrl entropy

$$S_W(\rho) = - \int Q(\alpha|\rho) \ln Q(\alpha|\rho) \frac{d\alpha^2}{\pi} \quad (22)$$

and the Fisher information

$$I(\rho) = \frac{1}{4} \int \frac{|\nabla Q(\alpha|\rho)|^2}{Q(\alpha|\rho)} \frac{d\alpha^2}{\pi}. \quad (23)$$

The quantity  $\mathcal{C}(\rho)$  captures the configurational trade-off between the spread (disorder) and localization (order) of the state in phase space. It is minimal ( $\mathcal{C} = 1$ ) for all displaced thermal states (including vacuum and coherent states) and increases with squeezing and photon number. Importantly, complexity can be large even when the Wigner function is completely non-negative (e.g., SV), thus revealing a form of structural richness that is independent of negativity. Wigner negativity and complexity can provide complementary insights to describe the phase space description of a given state in detail.

Since, the photon loss mechanism is same for all configuration, in below we only focus one some typical signal

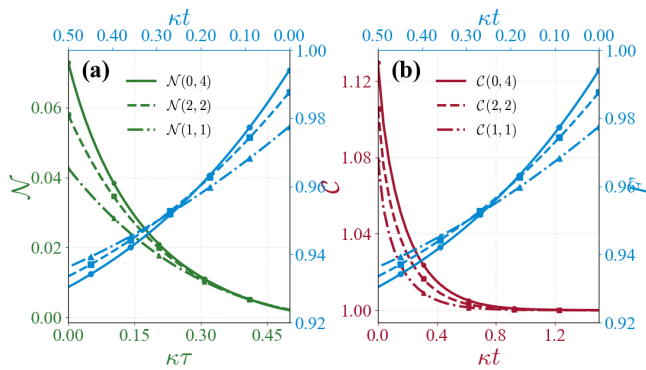


Figure 12. Changes of the fidelity  $F$ , Wigner negativity  $\mathcal{N}$ , and complexity  $\mathcal{C}$  of the heralded cubic-phase-state outputs for configurations (0, 4), (2, 2), and (1, 1) as functions of the photon loss rate  $\kappa t$ .

output states characterized by the configurations  $(m, n)$  which listed in Table I – Table IV.

We choose the (0, 4), (1, 1) and (2, 2) configurations to analyze the robustness of our approximated CPSs against pure photon loss arising from experimental imperfections; the numerical results are shown in Fig. 12. Our heralded output states are all good approximations to the ideal CPSs, with fidelities  $F = 0.997$  for (0, 4);  $F = 0.975$  for (1, 1) and  $F = 0.993$  for (2, 2) [see Table I].

In Fig. 12, we plot optical fidelity  $F$ , negativity  $\mathcal{N}$  and complexity  $\mathcal{C}$  of our signal output states  $|\Psi\rangle_{coh,m,n}$  (see Eq. 8) as a function of the single-photon loss rate  $\kappa t$ . The robustness against photon loss follows the ordering  $(0, 4) > (2, 2) > (1, 1)$ . Remarkably, the fidelity to the ideal CPS remains above 0.90 even for strong loss rates up to  $\kappa t = 0.50$ , indicating that our generated states exhibit strong resilience to single-photon loss—a favorable feature for their use in noisy quantum information processing environments.

From the negativity curves Fig. 12 (a), we observe that the negative regions of the Wigner functions for the selected configurations are small but nonzero. This implies that these states do not exhibit pronounced quantum interference fringes, consistent with their relatively modest non-classicality as measured by negativity. However, as shown in Fig. 12 (b), the initial complexities ( $\kappa t = 0$ ) are significant. As photon loss increases, the negativity gradually diminishes and vanishes for  $\kappa t > 0.50$ , indicating that the states become Gaussian-like in terms of their Wigner-function profile. Nevertheless, the complexity  $\mathcal{C}$  persists up to  $\kappa t = 1$ . This demonstrates that the structural complexity of our generated states can survive strong photon loss rates, even after the negative regions in phase space have entirely disappeared.

In Fig. 13 and 14, we plot the variations of the system quantities as functions of the single-photon loss rate  $\kappa t$  for the (1, 2) and (0, 2) configurations with an ECS input, and for (1,1), (1, 2) and (0, 2) configurations with an OCS input, respectively. The heralded output states

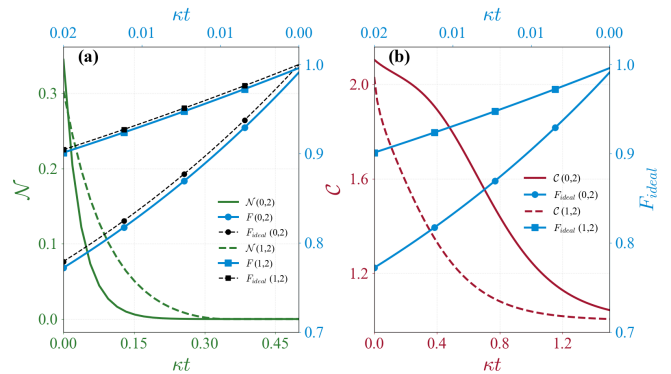


Figure 13. Changes of the fidelity  $F$ , Wigner negativity  $\mathcal{N}$ , and complexity  $\mathcal{C}$  of the heralded amplified cat states for even cat input under configurations (0, 2) and (1, 2) as functions of the photon loss rate  $\kappa t$ . The black curves represent the fidelity  $F_{ideal} = |\langle \Psi_\theta | \Phi_\theta \rangle|^2$  between the ideal squeezed cat state and its single-photon-loss counterpart for the same parameters (see main text for details)

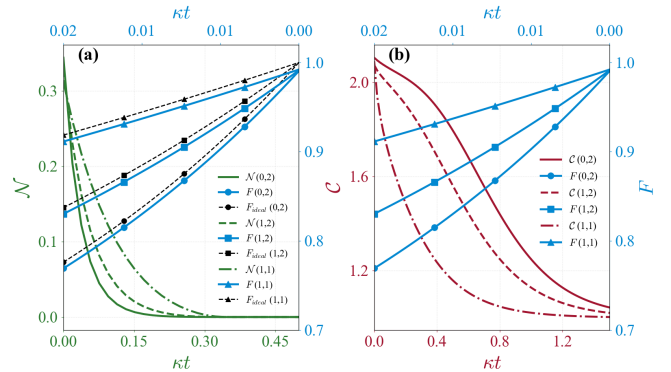


Figure 14. Changes of the fidelity  $F$ , Wigner negativity  $\mathcal{N}$ , and complexity  $\mathcal{C}$  of the heralded amplified cat states for odd cat input under configurations (0, 2), (1, 1) and (1, 2) as functions of the photon loss rate  $\kappa t$ . The black curves represent the fidelity  $F_{ideal}$  between the ideal squeezed cat state and its single-photon-loss counterpart for the same parameters.

corresponding to these configurations provide excellent approximations to the ideal squeezed cat states of the corresponding parity, with output amplitudes larger than 2.0 and extremely high fidelities ( $F \geq 0.99$ ) [see Table II and Table IV].

The robustness of these good approximations against photon loss, characterized by the fidelity  $F$  and the Wigner negativity  $\mathcal{N}$ , follows the ordering  $(1, 2) > (0, 2)$  for ECS input, and  $(1, 1) > (1, 2) > (0, 2)$  for OCS input. Among these, the (1, 2) and (1, 1) configurations—which effectively amplify small kitten states to large-amplitude ( $\alpha_{out} \geq 2.0$ ) squeezed cat states—exhibit excellent robustness, maintaining fidelity above 0.9 for  $\kappa t \leq 0.02$ . Although this loss window is narrower than that observed for the CPS cases [see Fig. 12], it is nevertheless a noteworthy performance for cat states, given their more com-

plex interference structures and higher sensitivity to decoherence.

The ordering of the complexity  $\mathcal{C}$  as a function of  $\kappa t$  is  $(0, 2) > (1, 2)$  for ECS inputs, and  $(0, 2) > (1, 2) > (1, 1)$  for OCS inputs. As shown in Fig. 13 and 14, these good approximations to amplified cat states exhibit relatively strong complexity  $\mathcal{C}$  and significantly more pronounced negativity  $\mathcal{N}$  compared to the CPS cases presented in Fig. 12. Interestingly, the complexity of these states persists even under very strong single-photon loss rates, long after the corresponding Wigner negativity has completely vanished.

For reference, we also plot the fidelity  $F_{ideal} = |\langle \Psi_\theta | \Phi_\theta \rangle|^2$  between the ideal squeezed Schrodinger cat state  $|\Psi_\theta\rangle$  [see Eq. (18)] and the squeezed Schrodinger cat state after a single-photon loss channel,  $|\Phi_\theta\rangle \propto a|\Psi_\theta\rangle$ , for same amplitude and squeezing parameters listed in Table II and Table IV. The results are shown in Fig. 13 (a) and 14 (a) as black curves. We observe that over the entire considered photon-loss range ( $0 \leq \kappa t \leq 0.02$ ), the discrepancy between our actual fidelity  $F$  and the ideal loss-channel fidelity remains below 1%. This indicates that our generated cat states retain structured phase-space distributions nearly identical to those of the ideal single-photon-loss case, and may remain operationally useful in lossy environments [59, 60].

## VI. CONCLUSION

In summary, we have proposed an OPA-based heralding framework that generates high-fidelity cubic phase states and amplifies Schrodinger cat states from  $\alpha_{in} \leq 1$

to  $\alpha_{out} \geq 2$  with  $F \geq 0.99$ , using both catalytic ( $m = n$ ) and non-catalytic ( $m \neq n$ ) configurations. The catalytic case preserves input parity and restores the idler state, while non-catalytic cases enable parity-flipping amplification with higher success probabilities. The amplified output can serve as a seed for subsequent rounds, providing a self-seeding pathway to progressively larger cat states. Requiring only moderate OPA gain and low-order photon detection, our protocol offers a flexible and experimentally accessible platform for non-Gaussian state engineering, with enhanced robustness against photon loss due to the squeezed nature of the output states.

Looking forward, our results suggest a practical route toward fault-tolerant continuous-variable quantum computation: the amplified squeezed cat states can serve as building blocks for GKP state preparation and bosonic error correction [3, 19, 55], while the ability to generate cubic phase states from coherent light provides a direct pathway to universal Gaussian-assisted quantum computation [61, 62]. Importantly, the self-seeding capability offers a scalable strategy for generating increasingly larger cat states without requiring progressively stronger squeezing or higher-order photon detection, potentially bridging the gap between currently available small-amplitude cat states and those required for practical fault-tolerant quantum information processing [63, 64].

## ACKNOWLEDGMENTS

This study was supported by the National Natural Science Foundation of China (No. 12365005).

- 
- [1] M. Walschaers, *PRX Quantum* **2**, 030204 (2021).
  - [2] T. Yoshida, D. Okuno, T. Kashiwazaki, T. Umeki, S. Miki, F. China, M. Yabuno, H. Terai, and S. Takeda, *PRX Quantum* **6**, 010311 (2025).
  - [3] A. L. Grimsmo and S. Puri, *PRX Quantum* **2**, 020101 (2021).
  - [4] Y. Zeng, F. Quijandria, C. Gneiting, and F. Nori, *Phys. Rev. Lett.* **136**, 190602 (2026).
  - [5] L. T. Knoll, A. G. Magnoni, and M. A. Larotonda, *Entropy* **27** (2025), 10.3390/e27070712.
  - [6] J. Liu, M. Zhang, H. Chen, L. Wang, and H. Yuan, *Adv. Quantum Technol.* **5**, 2100080 (2022).
  - [7] S. D. Huver, C. F. Wildfeuer, and J. P. Dowling, *Phys. Rev. A* **78**, 063828 (2008).
  - [8] X.-X. Zhang, Y.-X. Yang, and X.-B. Wang, *Phys. Rev. A* **88**, 013838 (2013).
  - [9] J. Sahota and N. Quesada, *Phys. Rev. A* **91**, 013808 (2015).
  - [10] P. A. Knott, T. J. Proctor, A. J. Hayes, J. P. Cooling, and J. A. Dunningham, *Phys. Rev. A* **93**, 033859 (2016).
  - [11] P. M. Anisimov, G. M. Raterman, A. Chiruvelli, W. N. Plick, S. D. Huver, H. Lee, and J. P. Dowling, *Phys. Rev. Lett.* **104**, 103602 (2010).
  - [12] D. Gottesman, A. Kitaev, and J. Preskill, *Phys. Rev. A* **64**, 012310 (2001).
  - [13] C. Weedbrook, S. Pirandola, R. García-Patrón, N. J. Cerf, T. C. Ralph, J. H. Shapiro, and S. Lloyd, *Rev. Mod. Phys.* **84**, 621 (2012).
  - [14] Y. Zheng, O. Hahn, P. Stadler, P. Holmval, F. Quijandria, A. Ferraro, and G. Ferrini, *PRX Quantum* **2**, 010327 (2021).
  - [15] S. U. Shringarpure and J. D. Franson, *Phys. Rev. A* **100**, 043802 (2019).
  - [16] O. Erkilic, A. Das, B. Shajilal, P. K. Lam, T. C. Ralph, and S. M. Assad, “A unified optical platform for non-gaussian and fault-tolerant gottesman-kitaev-preskill states,” (2025), arXiv:2512.02607 [quant-ph].
  - [17] X.-X. Yao, B. Zhang, and Y. Turek, *Phys. Rev. A* **113**, 033712 (2026).
  - [18] Y. Turek, M.-Y. Sun, and X.-X. Yao, “Multi-photon heralding generates large-amplitude squeezed schrödinger cat states and parity-selective fock superpositions from squeezed vacuum via an opa,” (2026), arXiv:2605.23617 [quant-ph].
  - [19] K. Fukui, A. Tomita, A. Okamoto, and K. Fujii, *Phys. Rev. X* **8**, 021054 (2018).

- [20] E. N. Bashmakova, S. B. Korolev, and T. Y. Golubeva, *Phys. Rev. A* **112**, 032434 (2025).
- [21] A. Ourjoumtsev, R. Tualle-Brouiri, J. Laurat, and P. Grangier, *Science* **312**, 83 (2006).
- [22] H. Takahashi, K. Wakui, S. Suzuki, M. Takeoka, K. Hayasaka, A. Furusawa, and M. Sasaki, *Phys. Rev. Lett.* **101**, 233605 (2008).
- [23] J. Johansson, P. Nation, and F. Nori, *Comput. Phys. Commun.* **184**, 1234 (2013).
- [24] A. E. Lita, A. J. Miller, and S. W. Nam, *Opt. Express* **16**, 3032 (2008).
- [25] D. Fukuda, G. Fujii, T. Numata, K. Amemiya, A. Yoshizawa, H. Tsuchida, H. Fujino, H. Ishii, T. Itatani, S. Inoue, and T. Zama, *Opt. Express* **19**, 870 (2011).
- [26] W. H. P. Pernice, C. Schuck, O. Minaeva, M. Li, G. N. Goltsman, A. V. Sergienko, and H. X. Tang, *Nat. Commun.* **3**, 1325 (2012).
- [27] T. Zhang, J. Huang, X. Zhang, C. Ding, H. Yu, Y. Xiao, C. Lv, X. Liu, Z. Wang, L. You, X. Xie, and H. Li, *Photon. Res.* **12**, 1328 (2024).
- [28] N. Jornod, M. Jankowski, L. M. Krüger, V. J. Wittwer, N. Modsching, C. Langrock, C. R. Phillips, U. Keller, T. Südmeyer, and M. M. Fejer, in *CLEO 2023* (Optica Publishing Group, 2023) p. STu3L.3.
- [29] K. Wakui, Y. Tsujimoto, M. Fujiwara, I. Morohashi, T. Kishimoto, F. China, M. Yabuno, S. Miki, H. Terai, M. Sasaki, and M. Takeoka, *Opt. Express* **28**, 22399 (2020).
- [30] R. A. Brewster, I. C. Nodurft, T. B. Pittman, and J. D. Franson, *Phys. Rev. A* **96**, 042307 (2017).
- [31] P. Marek, H. Jeong, and M. S. Kim, *Phys. Rev. A* **78**, 063811 (2008).
- [32] J. Park, J. Joo, A. Zavatta, M. Bellini, and H. Jeong, *Opt. Express* **24**, 1331 (2016).
- [33] J. FadrnÅoe, M. Neset, M. Bielak, M. JeÅYek, J. BÅ-lek, and J. FiurÅjÅjek, *npj Quantum Information* **10**, 89 (2024).
- [34] O. Erkilic, A. Das, B. Shajilal, P. K. Lam, T. C. Ralph, and S. M. Assad, "A unified optical platform for non-gaussian and fault-tolerant Gottesman-Kitaev-Preskill states," (2025), arXiv:2512.02607 [quant-ph].
- [35] T. Gerrits, S. Glancy, T. S. Clement, B. Calkins, A. E. Lita, A. J. Miller, A. L. Migdall, S. W. Nam, R. P. Mirin, and E. Knill, *Phys. Rev. A* **82**, 031802(R) (2010).
- [36] S. Lloyd and S. L. Braunstein, *Phys. Rev. Lett.* **82**, 1784 (1999).
- [37] F. Arzani, N. Treps, and G. Ferrini, *Phys. Rev. A* **95**, 052352 (2017).
- [38] M. Yukawa, K. Miyata, H. Yonezawa, P. Marek, R. Filip, and A. Furusawa, *Phys. Rev. A* **88**, 053816 (2013).
- [39] R. Yanagimoto, T. Onodera, E. Ng, L. G. Wright, P. L. McMahon, and H. Mabuchi, *Phys. Rev. Lett.* **124**, 240503 (2020).
- [40] H. Kashyap, D. A. Kopylov, and P. R. Sharapova, *Laser Physics Letters* **23**, 045209 (2026).
- [41] Y. Miwa, J.-i. Yoshikawa, N. Iwata, M. Endo, P. Marek, R. Filip, P. van Loock, and A. Furusawa, *Phys. Rev. Lett.* **113**, 013601 (2014).
- [42] D. V. Sychev, A. E. Ulanov, A. A. Pushkina, M. W. Richards, I. A. Fedorov, and A. I. Lvovsky, *Nature Photonics* **11**, 379 (2017).
- [43] A. P. Lund, H. Jeong, T. C. Ralph, and M. S. Kim, *Phys. Rev. A* **70**, 020101(R) (2004).
- [44] Q. Xu, G. Zheng, Y.-X. Wang, P. Zoller, A. A. Clerk, and L. Jiang, *npj Quantum Inf.* **9**, 78 (2023).
- [45] J. FiurÅsek, S. Grebien, and R. Schnabel, *Phys. Rev. A* **111**, 043704 (2025).
- [46] N. Wang, X. Zhang, Q. Liu, F. Sun, Q. He, and Y. Gu, *J. Opt. Soc. Am. B* **42**, 939 (2025).
- [47] H. Song, G. Zhang, X. Wang, H. Yonezawa, and K. Fan, *Phys. Rev. A* **105**, 043713 (2022).
- [48] K. Takase, J.-i. Yoshikawa, W. Asavanant, M. Endo, and A. Furusawa, *Phys. Rev. A* **103**, 013710 (2021).
- [49] M. Eaton, R. Nehra, and O. Pfister, *New Journal of Physics* **21**, 113034 (2019).
- [50] X.-X. Yao and Y. Turek, *Quantum Sci. Technol.* **11**, 025038 (2026).
- [51] X.-X. Yao and Y. Turek, *npj Quantum Inf.* **12**, 30 (2026).
- [52] M. Yukawa, K. Miyata, T. Mizuta, H. Yonezawa, P. Marek, R. Filip, and A. Furusawa, *Opt. Express* **21**, 5529 (2013).
- [53] H. Luo and S. Mahmoodian, *Phys. Rev. Appl.* **25**, 024046 (2026).
- [54] K. Huang, H. Le Jeannic, J. Ruauadel, V. B. Verma, M. D. Shaw, F. Marsili, S. W. Nam, E. Wu, H. Zeng, Y.-C. Jeong, R. Filip, O. Morin, and J. Laurat, *Phys. Rev. Lett.* **115**, 023602 (2015).
- [55] D. S. Schlegel, F. Minganti, and V. Savona, *Phys. Rev. A* **106**, 022431 (2022).
- [56] S. Kiryu, K. Fukui, A. Okamoto, and A. Tomita, *Phys. Rev. A* **112**, 042615 (2025).
- [57] A. Kenfack and K. Życzkowski, *J Opt B Quantum Semi-classical Opt* **6**, 396 (2004).
- [58] S. Tang, F. Albarelli, Y. Zhang, S. Luo, and M. G. A. Paris, *Quantum Sci. Technol.* **10**, 045047 (2025).
- [59] Y. S. Teo, S. U. Shringarpure, S. Cho, and H. Jeong, *Quantum Science and Technology* **10**, 035003 (2025).
- [60] S. B. Korolev and T. Y. Golubeva, *Phys. Rev. A* **113**, 022413 (2026).
- [61] S. L. Braunstein and P. van Loock, *Rev. Mod. Phys.* **77**, 513 (2005).
- [62] M. Walschaers, B. Sundar, N. Treps, L. D. Carr, and V. Parigi, *Quantum Sci. Technol* **8**, 035009 (2023).
- [63] P. Renault, P. Yard, R. C. Pooser, M. Eaton, and H. A. Zaidi, *Quantum* **9**, 1796 (2025).
- [64] L. D. H. My, S. Qin, and H. K. Ng, *Quantum* **9**, 1810 (2025).